Large Eddy Simulation of Air Entrainment and Mixing in Reacting and Non-Reacting Diesel Sprays

Cheng Gong · Mehdi Jangi · Tommaso Lucchini · Gianluca D'Errico · Xue-Song Bai

Received: 20 December 2013 / Accepted: 11 August 2014

1 Introduction

In diesel spray combustion ambient air entrainment provides the high temperature gas for evaporating liquid spray and oxygen for initiating the subsequent combustion and formation of pollutants such as NOx and soot. Spray/air mixing is a consequence of several processes, e.g., spray breakup, evaporation, and turbulence mixing, which are affected by combustion heat release. These processes interact with one another in a highly nonlinear way. The shear

C. Gong · M. Jangi · X.-S. Bai (✉)
Division of Fluid Mechanics, Department of Energy Sciences, Lund University,
SE-221 00 Lund, Sweden
e-mail: xue-song.bai@energy.lth.se

T. Lucchini · G. D'Errico
Department of Energy, Politecnico di Milano, I-20156 Milan, Italy

force between the high-speed spray and the ambient gas triggers instability of the shear layer, which results in transition to turbulence. Subsequently, air is entrained into spray by the roll-up of eddies. The characteristics of air entrainment into fuel jets have been studied since the early work of Ricou and Spalding [1]. For diesel spray jet, particle image velocimetry (PIV) technique has been widely used to measure the velocity field [2–6]. Sasaki et al. [2] found that, in a non-evaporating condition, a rather small amount of air was entrained near the nozzle and a large amount of air entrainment occurred in the spray mid-section and the tip. Measurements on non-evaporating spray by Rhim and Farrell [4] showed that there was a large difference between the total spray volume and the accumulated volume of the entrained gas across the cross-sections of the spray jet; they concluded that a significant portion of the total entrained gas into the transient sprays was entrained from the spray tip. Their other studies on the evaporating [5] and combusting [6] diesel sprays showed that the normal and tangential velocities on the jet surface were in general larger than those of non-evaporating spray conditions.

A parameter often measured in the diesel jet is the transient spray tip penetration. A scaling law for the penetration of a non-vaporizing fuel jet was developed by Naber and Siebers [7]. Siebers [8] reviewed experimental results on jet penetration under conditions relevant to direct injection diesel engines, and compared the experimental penetration with the scaling law. It was shown that the non-reacting vaporizing spray penetrated slower than the non-vaporizing spray, and the combusting fuel jets penetrated faster than the vaporizing fuel jets. Contrary to this, recent measurements on liquid and vapor penetration reported by the Engine Combustion Network (ECN) show rather similar vapor penetration lengths in the vaporizing but non-reacting spray and combusting spray under otherwise similar conditions [9]. Despite the significant recent progress in understanding of spray/air mixing, there is still a need to look into this process in more complex conditions such as diesel flames. In particular, how the combustion, including the low temperature chemistry upstream of the lift-off position, affects the air entrainment and mixing with the fuel is not clear.

Simultaneous measurement of key parameters, e.g., flow velocities and species mass fractions, are needed to understand the details of the mixing process in diesel spray combustion. Preferably, heat release rate in the combusting spray may be measured to aid in the understanding of the effect of heat release on the flow, fuel evaporation, and the mixing process. This is difficult to achieve in experiments, especially for the combusting diesel spray. Computational fluid dynamics (CFD) has been shown a powerful tool in the recent research of the diesel spray combustion. Large eddy simulation (LES) offers a unique compromise between computational cost and accuracy of spray simulation since it captures the development of the unstable shear layer between the fuel flow and the ambient air. Zhou et al. [10] compared LES and simulations based on the framework of Reynolds averaged Navier-Stokes (RANS) for a diesel engine. LES, which can capture the complex vortex structures of turbulent spray field, predicts the flow and spray characteristics in better agreement with experimental data than RANS. Solsjö and Bai [11] examined the sensitivity of the spray model parameters used in a LES simulation under a diesel-like condition with high injection pressure. It was shown that the liquid penetration length, the flow velocity and vapor distribution in the near-nozzle region were moderately sensitive to the model parameters; moreover, the vapor penetration and distribution of vapor fuel in the downstream region was rather insensitive to the model parameters.

In the present study, LES is employed to simulate the evolution of reacting and non-reacting diesel sprays under a nearly identical ambient density and temperature conditions. The studied cases are known as the ECN Spray A cases with n-dodecane as fuel. The

objective of this study is to improve the understanding of the air entrainment and the mixing process the diesel sprays under reacting and non-reacting conditions.

2 LES Spray Combustion Model and Case Setup

Eulerian–Lagrangian coupling method is used for spray modeling. In the LES framework, spatially filtered conservation equations for the gas phase can be written as:

$$\frac{\partial \bar{\rho}}{\partial t} + \frac{\partial \bar{\rho}\tilde{u}_j}{\partial x_j} = \bar{S}^s_\rho, \tag{1}$$

$$\frac{\partial \bar{\rho}\tilde{u}_i}{\partial t} + \frac{\partial}{\partial x_j}\left[\bar{\rho}\tilde{u}_j\tilde{u}_i - \bar{\tau}_{ij} - \tau^{sgs}_{ij}\right] = \bar{S}^s_{u_i}, \tag{2}$$

$$\frac{\partial \bar{\rho}\tilde{Y}_i}{\partial t} + \frac{\partial \bar{\rho}\tilde{u}_j\tilde{Y}_i}{\partial x_j} - \frac{\partial}{\partial x_j}\left[\bar{\rho}\tilde{D}\frac{\partial \tilde{Y}_i}{\partial x_j} + \Phi^{sgs}_{Y_i}\right] = \bar{S}^s_{Y_i} + \widetilde{\dot{\omega}_i}, \tag{3}$$

$$\frac{\partial \bar{\rho}\tilde{h}_s}{\partial t} + \frac{\partial \bar{\rho}\tilde{u}_j\tilde{h}_s}{\partial x_j} - \frac{\partial}{\partial x_j}\left[\bar{\rho}\tilde{\alpha}\frac{\partial \tilde{h}_s}{\partial x_j} + \Phi^{sgs}_{h_s}\right] = \bar{S}^s_h - \sum_{i=1}^{N_s}\widetilde{\dot{\omega}_i}h^0_{f,i}, \tag{4}$$

$$\frac{\partial \bar{\rho}\tilde{Z}}{\partial t} + \frac{\partial \bar{\rho}\tilde{u}_j\tilde{Z}}{\partial x_j} - \frac{\partial}{\partial x_j}\left[\bar{\rho}\tilde{D}\frac{\partial \tilde{Z}}{\partial x_j} + \Phi^{sgs}_{Z}\right] = \bar{S}^s_Z. \tag{5}$$

The overlines denote the spatial filtering

$$\overline{\phi(x,t)} = \int G(r,x)\phi(x-r,t)dr, \tag{6}$$

where the integration is over the entire field and the filter function G satisfies the normalization condition, $\int G(r,x)dr = 1$. Tilde denotes the density weighted spatial filtering, $\overline{\rho\phi} = \bar{\rho}\tilde{\phi}$, also known as Favre filtering.

In Eqs. 1–5, ρ is density; u is velocity; Y_i is the mass fraction of the ith species; h_s is the sensible enthalpy; $\dot{\omega}_i$ is the chemical reaction rate for the ith species; $h^0_{f,i}$ is the enthalpy of formation for the ith species; Z is mixture fraction; α and D are diffusion coefficients of heat and mass, respectively. Superscript s denotes the spray and sgs denotes the sub-grid variables. $\bar{S}^s_\rho$, $\bar{S}^s_{u_i}$, $\bar{S}^s_{Y_i}$, $\bar{S}^s_{h_s}$ and $\bar{S}^s_Z = \bar{S}^s_\rho$ are source terms that account for the exchange rate of mass, momentum, and energy between the gas and liquid phases. $\bar{\tau}_{ij}$ is filtered stress tensor obtained from the resolved strained rate $\tilde{S}_{ij}$, using

$$\bar{\tau}_{ij} = -\bar{p}\delta_{ij} + 2\bar{\mu}\tilde{S}_{ij} + 1/3\tilde{S}_{kk}\delta_{ij}. \tag{7}$$

Terms τ^{sgs}, $\Phi^{sgs}_{Y_i}$, Φ^{sgs}_h and Φ^{sgs}_Z require further modeling in order to close the set of Eqs. 1–5. The sub-grid stress τ^{sgs} tensor is modeled using a one-equation eddy model,

$$\tau^{sgs} = 2\bar{\rho}\upsilon^{sgs}(\tilde{S}_{ij} - 1/3\tilde{S}_{kk}\delta_{ij}) - 2/3\bar{\rho}k^{sgs}\delta_{ij}, \tag{8}$$

with the sub-grid eddy viscosity $\upsilon^{sgs} = C_\upsilon\sqrt{k^{sgs}}/\bar{\Delta}$ and $\bar{\Delta} = V^{1/3}_{cell}$, where V_{cell} is the volume of local mesh cell. The sub-grid kinetic energy k^{sgs} is obtained from a transport equation [12]:

$$\frac{\partial \bar{\rho}k^{sgs}}{\partial t} + \frac{\partial \bar{\rho}\tilde{u}_j k^{sgs}}{\partial x_j} = \tau^{sgs}\frac{\partial \tilde{u}_j}{\partial x_j} - D^{sgs} + \frac{\partial}{\partial x_j}\left[\bar{\rho}\frac{\upsilon^{sgs}}{\sigma_k}\frac{\partial k^{sgs}}{\partial x_j}\right] + \dot{W}^s, \tag{9}$$

where $\dot{W}^s$ is the spray-induced turbulence source term [13]. The sub-grid heat and species mass fluxes are modelled using the gradient-diffusion closure,

$$\Phi_{h_s}^{sgs} = \bar{\rho}\frac{\upsilon^{sgs}}{Pr^{sgs}}\frac{\partial \tilde{h}_s}{\partial x_j},\ \Phi_{Y_i}^{sgs} = \bar{\rho}\frac{\upsilon^{sgs}}{Sc^{sgs}}\frac{\partial \tilde{Y}_i}{\partial x_j},\ \Phi_Z^{sgs} = \bar{\rho}\frac{\upsilon^{sgs}}{Sc^{sgs}}\frac{\partial \tilde{Z}}{\partial x_j}, \tag{10}$$

where $Pr^{sgs} = 0.7$ and $Sc^{sgs} = 0.7$ are the sub-grid Prandtl number and Schmidt number, respectively.

The spray source terms in Eqs. 1–5 are obtained using Lagrangian particle tracking (LPT) approach. In this approach spray is considered as discrete phase consisting of a large number of evaporating droplets. The droplet is not tracked individually in a Lagrangian framework. The number of droplets in sprays is massively large, thus, tracking every single droplet is not computationally feasible. An efficient way is to describe the sprays as a limited number of parcels; within each parcel the droplets have identical physical properties, e.g., size and temperature. Lagrangian tracking is performed for the parcels instead of individual droplets. Equations of motion for a parcel are

$$\frac{d}{dt}\vec{x}_p = \vec{u}_p, \tag{11}$$

$$\frac{d}{dt}\vec{u}_p = \frac{C_D}{\tau_p}\frac{Re_p}{24}(\vec{u}_g - \vec{u}_p) = \frac{C_D}{\tau_p}\frac{Re_p}{24}\vec{u}_{rel}. \tag{12}$$

Here, $\vec{x}_p$ is the parcel position vector, $\vec{u}_p$ is the parcel velocity, $\vec{u}_g$ is the surrounding gases velocity, C_D is the drag coefficient. $\tau_p = d_p^2/18\bar{\upsilon}$ is the parcel characteristic time, where d_p is the diameter of the parcel, $\bar{\upsilon}$ is the gas-phase kinematic viscosity. The parcel Reynolds number is defined as $Re_p = |\vec{u}_{rel}|\, d_p/\bar{\upsilon}$, where $\vec{u}_{rel} = \vec{u}_g - \vec{u}_p$ is the relative velocity between the parcel and the surrounding gas. The drag coefficient C_D is calculated as

$$C_D = \begin{matrix} \frac{24}{Re_p}\ \ 1 + \frac{1}{6}Re_p^{2/3}\Big), & Re_p \le 1000 \\ 0.426, & Re_p > 1000 \end{matrix} \tag{13}$$

The instantaneous relative velocity between the parcels and the surrounding gas, $\vec{u}_{rel}$, is not readily known and thus it requires closure. Here, we use O'Rourke's model [14] to estimate $\vec{u}_{rel}$. This model in LES formulation is written as

$$\vec{u}_{rel} = \vec{\tilde{u}} + \vec{u'}_p - \vec{u}_p \tag{14}$$

where $\vec{\tilde{u}}$ is local Favre-filtered velocity of the gas phase, and $\vec{u'}_p$ is stochastic velocity vector of the parcel accounting for turbulence dispersion via interaction with the surrounding gas. $\vec{u'}_p$ is assumed to have a Gaussian distribution with variance $\sigma = \sqrt{2k^{sgs}/3}$ and a mean of zero. In this way each component of $\vec{u'}_p$ is chosen randomly from the Gaussian distribution function

$$G(u'_{p,i}) = \frac{1}{\sigma\sqrt{2\pi}}\exp\left(-\frac{u'_{p,i}}{2\sigma}\right)^2 \tag{15}$$

The momentum source term in Eq. 2, $\bar{S}_{u_i}^s$, can be obtained from

$$\bar{S}_{u_i}^s = \frac{1}{V_{cell}}\sum\left(m_p\frac{d}{dt}u_{p,i}\right), \tag{16}$$

where the summation is over total number of parcels that crossed V_{cell} during the Eulerian time step. $\bar{S}^s_\rho$ and $\bar{S}^s_h$ are obtained similarly. The spray-induced turbulence source term in Eq. 9 is closed with the following model [13]

$$\dot{W}^s = \frac{1}{V_{cell}} \sum \left(m_p \frac{d}{dt} \vec{u}_p \right) \cdot \left(2\vec{\tilde{u}} - 3\vec{\tilde{\tilde{u}}} + \vec{\tilde{\tilde{\tilde{u}}}} \right), \tag{17}$$

where $\vec{\tilde{\tilde{u}}}$ and $\vec{\tilde{\tilde{\tilde{u}}}}$ are double and triple Favre-filtered velocity vector, respectively.

Models are needed to describe the evaporation and breakup of the parcels. The Ranz-Marshall correlation was used to compute droplet heat transfer with the surrounding gas phase and evaporation was modeled using Frossling equations. The Huh-Gosman model [15] and Kelvin-Helmholtz (WAVE) model [16] were used for the primary and the secondary breakup, respectively. Further details on the models for the discrete phase are given in Appendix A. Collision and coalescence were not taken into account since they have a minimum influence when evaporating spray is considered [17]. Validation of the present Eulerian–Lagrangian method for the spray simulation within the RANS and LES frameworks can be found in Ref. [18–20].

As both turbulence and detailed chemistry play important role in the ignition and combustion process of diesel spray, models are needed to take into account turbulence and chemistry interaction. Recently, several authors have reported simulations using different models. One of the baseline models is the well-stirred reactor (WSR) model that can easily incorporate detailed chemistry into the simulation and hence is often used in engine combustion simulations, cf. Ref. [21] and the references therein. Other models often used are flamelet models and transported probability density function (PDF) models. Using an unsteady flamelet progress variable (UFPV) model, Bajaj et al. [22] reported RANS simulations of auto-ignition and flame lift-off in diesel jets of the n-heptane and n-dodecane experimentally studied within ECN [9]. The model was shown to predict the ignition delay and the flame lift-off within 25 % of the experimental values. D'Errico et al. [18] compared the simulations with the flamelet model and with the WSR model for the n-dodecane spray jet cases of ECN (Spray A cases). The ignition delay time predicted with the WSR model agrees well with the flamelet model; however, both models over-predict the ignition delay time as compared with the experiments. The flamelet model predicts the flame lift-off height in closer agreement with the experimental values than the WSR model does. Bhattacharjee and Haworth [23] and Pei et al. [21, 24] compared the simulations of the ECN diesel jet cases with transported PDF model and the WSR model. The WSR model and the PDF model predict comparable ignition delay time, whereas the PDF model predicted the flame lift-off height in closer agreement with the experiments than the WSR model does. Pei et al. [21] show that the uncertainties in the chemical kinetics and in the mixing sub-models of the PDF approach can result in equally large discrepancies between the simulation results as that between the WSR model and the PDF model.

The WSR model is chosen here based on the above-discussed studies. It has been shown that the RANS based WSR model often predicts much thinner mean reaction zones than other models, e.g. the transported PDF model [21, 23]. In the present LES study, this is expected a less serious problem owing to broadening of the reaction zones by the unsteady motion of the coherent structures and turbulence resolved in LES.

To integrate the source terms due to elementary reactions in the species transport and energy equations, a recently developed computation acceleration method, the so-called chemistry coordinate mapping (CCM) method [25–28], is employed. The basic idea of the CCM method is to map the thermo-chemistry identical points in the physical space to a point

in a multidimensional phase space made up of temperature, $\tilde{T}$, mass fraction of H-atom, J_H, and a logarithm function of the scalar dissipation rate, $\alpha = \log_{10}(\nabla J_H \cdot \nabla J_H + 1)$. In general, there are multiple physical space points mapped to one phase space point, which results in a speed up of numerical integration of the chemical reaction rates. This method has been applied to direct numerical simulations (DNS) of premixed and partially premixed combustion [25, 28], RANS of diesel spray combustion [26], LES of diesel Engine combustion [29], and recently to transport PDF method [30]. In the present reacting case, the speedup is about a factor of 30. Further details of the CCM setup used in this work can be found in Appendix B.

OpenFOAM [31] is used for numerical solution of the governing equations. In particular, second order finite-volume schemes are used for the spatial discretization (with the so-called filtered linear scheme) and temporal integration (with the backward Euler scheme).

Two baseline cases of the Sandia Constant Volume Vessel experiments (the ECN Spray-A cases) are simulated. In both cases the fuel is n-Dodecane and the ambient gas is initially at 900 K with a density of 22.8 kg/m^3 [9]. The injector pressure drop is 150 MPa and the injector nozzle diameter is 90 μm. The injection duration is 6 ms. Table 1 lists the initial compositions of the ambient gases. A skeletal kinetic mechanism for n-Dodecane [32] was used; the mechanism is made up of 103 species and 370 reactions.

The computational domain is a cube with 108 mm at each side, the same size as the combustion chamber in the experiment. Initial velocity of the ambient gas was set to zero. All boundaries of the domain were set as non-slip wall; temperature on the boundaries was assumed to be a constant of 900 K. The liquid fuel is injected from the center of the bottom plane, the (x, y)-plane, of the domain along z-direction. Based on previous parcel and grid sensitivity studies [11, 18], the total number of parcels and grid resolution are determined. The total mass of the liquid fuel (about 14 mg) is described as 5×10^5 parcels in the simulation. A fine mesh with the grid size of 0.25 mm was used near the nozzle to capture the strong turbulence induced by the jet. The mesh is coarsened near the walls. In total, 1.36 million cells are used. This mesh was shown to provide reasonably accurate results. The computation took 46000 cpu hours for the reacting spray case.

3 Results and Discussion

Figure 1 shows the temporal evolution of pressure rise in the vessel, p-p_0, where p_0 is the initial pressure. The vessel pressure in the non-reacting case decreases slightly during the injection stage because of cooling of the ambient gas as the spray is evaporating. For the reacting case, the initial evolution of the pressure is similar to that in the non-reacting case until the onset of auto-ignition; thereafter, the vessel pressure increases monotonically with time due to the heat release from combustion. In the main combustion period, which is mixing controlled diffusion flame, the pressure-rise slope predicted numerically agrees well with the experimental one. The ignition delay time in the numerical simulation is however over-predicted; it was over-predicted also in the studies with flamelet models and transported

Table 1 Composition of the ambient gas (in mole fraction) [9]

Cases	O_2	N_2	CO_2	H_2O
Non-reacting	0	0.8971	0.0652	0.0377
Reacting	0.15	0.7515	0.0623	0.0362

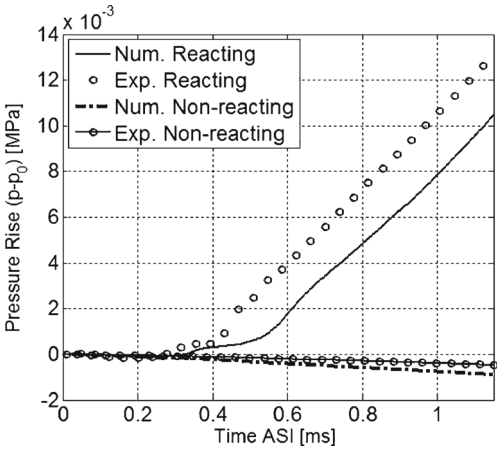

Fig. 1 Temporal evolution of the pressure-rise in the constant volume vessel. Experimental data are taken from Ref. [9]

PDF models [18, 21, 23]; hence, one may speculate that the over-prediction of the ignition delay time can be partly due to uncertainties in the chemical kinetics.

Figure 2 shows the penetrations of the liquid spray and the vapor fuel. The recommended definition from ECN [9] is employed to calculate the lengths of liquid and vapor penetration. The liquid penetration is defined as the maximum distance from the nozzle to the farthest axial position with 0.1 % liquid volume fraction, averaged over a cylindrical volume of 1 mm in diameter and 1 mm in axial length; vapor penetration is determined using the farthest downstream location of 0.1 % fuel mass fraction (or mixture fraction for the reacting case). The liquid length was not measured in the reacting experiment. The penetration lengths agree well with the experiment for both the reacting and non-reacting cases. The simulations show that the liquid length in the reacting case is slightly shorter than that in the non-reacting case after 0.3 ms after the start of injection (ASI); the mean liquid lengths between 0.3 ms and 1.2 ms ASI are 10.2 mm and 7.9 mm for the non-reacting and reacting spray, respectively. The predicted vapor phase penetration is somewhat longer than that in the non-reacting case after the onset of high temperature ignition, in particular after 1.0 ms ASI. This trend is consistent with the experimental results summarized in Ref. [8]. A slight difference in the penetration length between the reacting and non-reacting sprays can also be identified in the presently studied ECN experimental results.

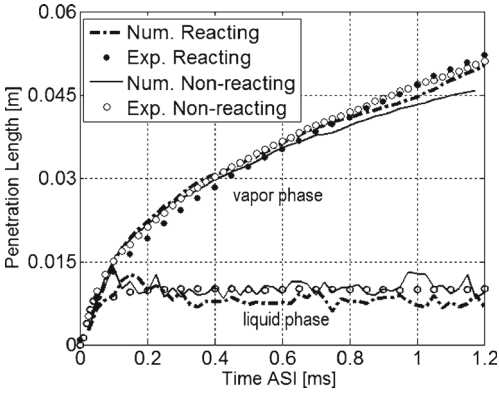

Fig. 2 Penetration lengths of the liquid and fuel vapor. Experimental data are taken from Ref. [9]

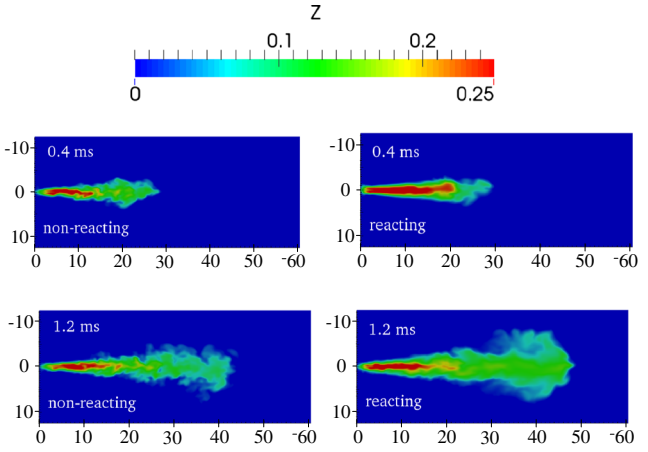

Fig. 3 Distributions of mixture fraction in an axisymmetric plane at 0.4 ms and 1.2 ms ASI The axis scale is in millimeters (mm)

Figure 3 shows the distribution of mixture fraction (Z) in an axisymmetric plane of the jet at 0.4 ms (before the high temperature ignition) and 1.2 ms (after the high temperature ignition) ASI. A comparison of the reacting and non-reacting spray cases shows that the spreading of the spray in radial direction in the two cases is nearly the same before the high temperature ignition. Later on, mixture fraction in the reacting spray case spreads to larger domain than the non-reacting case (1.2 ms in the figure), in both the axial and radial directions. To investigate the difference in transport of the mixture in the radial direction, the mean radial velocity of the gas phase is shown Fig. 4. The mean radial velocity is obtained by carrying out time-average between 1.0 ms and 2.0 ms ASI. During this period the upstream part of the transient jet has already reached to the statistical steady state. It is clearly shown that the radial velocity in the reacting case is higher than that in the non-reacting case, which results in faster transport of fuel vapor in the radial direction. The higher radial velocity in the reacting spray is a result of hot gas expansion. For the same reason hot gas expansion from the lifted flame speeds up the vapor gas penetration in axial direction. This will be discussed further later.

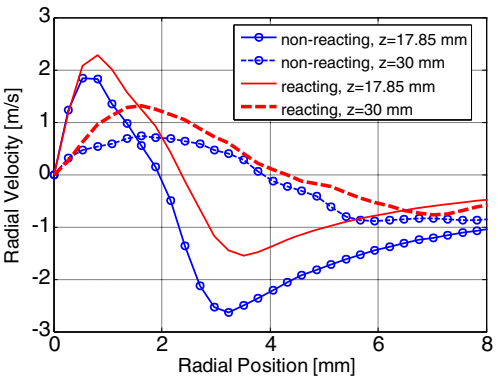

Fig. 4 Mean radial velocity at two axial positions, 17.85 mm and 30 mm above the nozzle exit plane

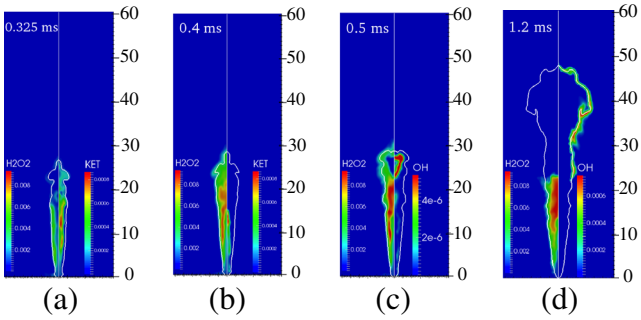

Fig. 5 Snapshots of some key variables at several instantaneous times ASI. The stoichiometric mixture is shown with white lines in the figure (the *left* and *right* side on each frame are from the same side in the axisymmetric plane)

To illustrate the ignition process of the reacting spray 2D distributions of several key species are plotted in Fig. 5. The reacting spray undergoes a two-stage ignition process. The disappearance of ketohydroperoxide (KET) and the formation of H_2O_2 between 0.325 ms and 0.4 ms ASI indicate the onset of the first-stage ignition (low temperature ignition) [33]; the disappearance of H_2O_2 and the formation of OH at the tip of the fuel jet at 0.5 ms indicate the onset of high temperature ignition. After the high temperature ignition, a lifted diffusion flame is formed as indicated by the OH distribution at 1.2 ms ASI. The lift-off height, which is defined as the axial distance from the fuel nozzle to the nearest axial location with its local OH mass fraction reaching to 2 % of its maximum in the domain, is about 21 mm in present simulation. It is worthy noting that the structure of the low temperature ignition region and the species distribution (referred to as "cool flame" in the later discussion) are preserved after the high temperature ignition.

To investigate the effect of combustion on the density and temperature fields, Fig. 6 shows snapshots of density and temperature at 0.4 ms and 1.2 ms ASI. It is shown that both the lifted flame and the cool flame can affect the density and temperature noticeably. In the cool flame region, combustion decreases the density from around 35 kg/m^3 (in the non-reacting spray) to around 25 kg/m^3 (in the reacting spray), and increases the temperature from around 800 K to around 1000 K (in the reacting spray); in the lifted flame region, combustion decreases the density from around 30 kg/m^3 (in the non-reacting spray) to around

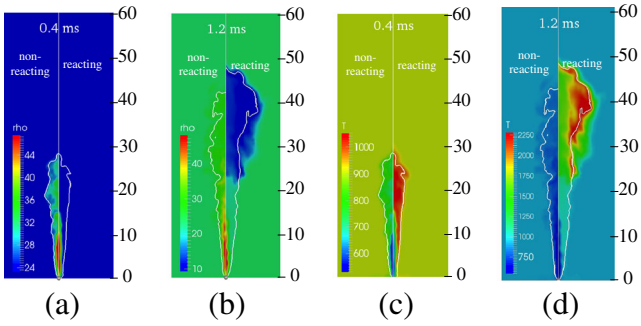

Fig. 6 Snapshots of density (**a**, **b**) and temperature (**c**, **d**) from the non-reacting and reacting sprays at two instantaneous times ASI

10 kg/m^3 (in the reacting spray), and increases the temperature from around 800 K to above of 2000 K (in the reacting spray).

Figure 7 shows the scatter plots of the temperature (T) in the flow field as a function of the local mixture fraction (Z). In the non-reacting spray, the distribution of temperature in Z space contains two branches that meet each other at 585 K with the maximal mixture fraction in the domain. This temperature is approximately the boiling temperature of the fuel under the present ambient pressure. The vapor fuel on the upper branch comes from the boiling droplets at the boiling temperature near the nozzle in the physical space, so the

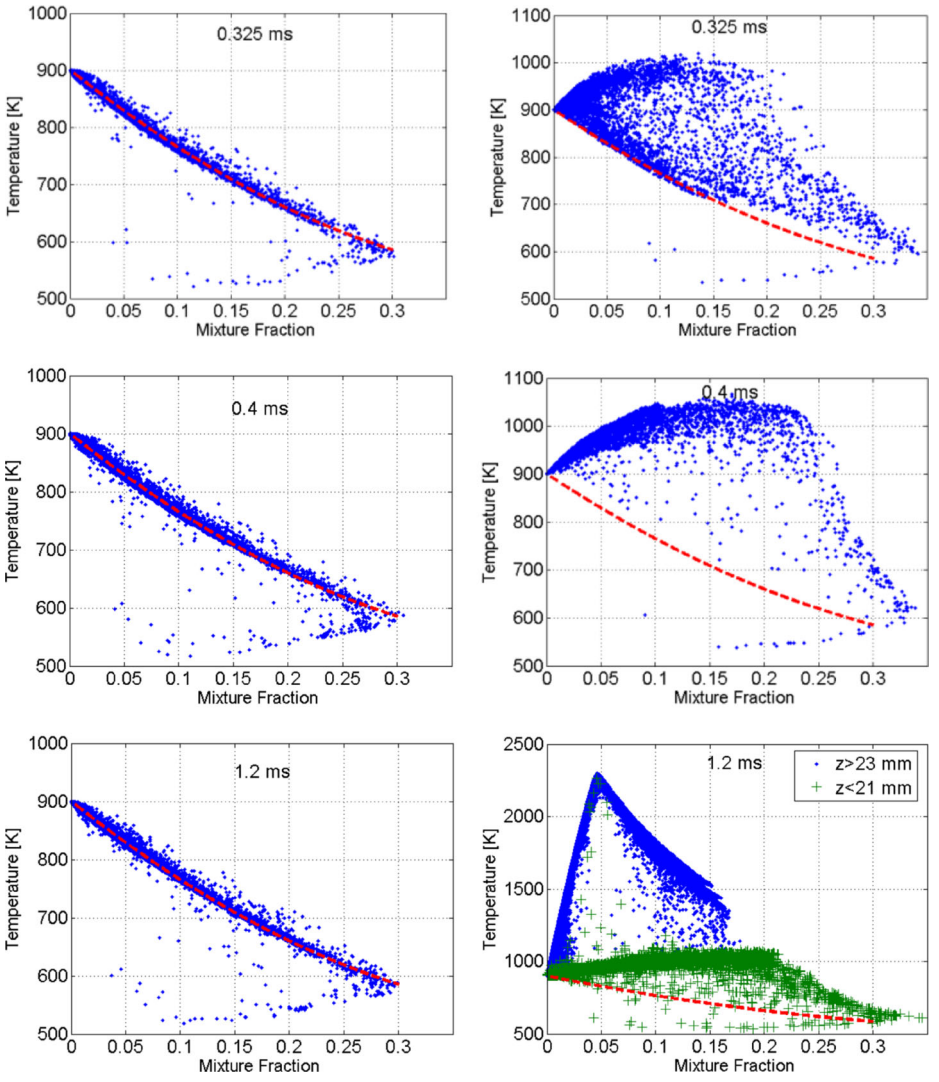

Fig. 7 Scatter plot of the temperature with the mixture fraction, based on all points in the flow field. *Dashed lines*: analytic fitting function based on the non-reacting case

local temperature decreases with the mixture fraction when the fuel mixes with the high temperature air. The vapor fuel on the lower branch comes from the droplets with their temperature below the boiling point. The evaporation of these droplets is not due to boiling. Their evaporation rate increases with the temperature, so the local mixture fraction increases with the temperature on this branch. The distribution of temperature in phase space changes rather little in the non-reacting case; the change occurs mainly in the lower branch, which corresponds to the near nozzle region in the physical space.

A quadratic function is found to fit the relation between temperature and mixture fraction for the mixture on the upper branch in the non-reacting case,

$$T = 1500Z^2 - 1500Z + T_{am} \tag{18}$$

where T_{am} is the ambient temperature (900 K in the present cases). This fitting function is plotted together with the scatter plots for both the non-reacting and the reacting cases in Fig. 7 (shown as the red dashed lines in the figure). The relation between the temperature and mixture fraction in the present non-reacting jet is different from that of the gas fuel jet, which is usually known as a linear relation between the temperature and mixture fraction if the Lewis number of the fuel is close to unity. The difference is due to the evaporation of the liquid fuel, which results in a loss of heat into the surrounding gas.

The temperature scattering in the phase space is very different in the two cases at the early time (0.325 ms ASI), which is about the onset of the first-stage ignition in the reacting case. A comparison between the scatter plot of the reacting case with the fitting function for the non-reacting case shows that the mixture in the reacting case has a similar temperature distribution to that in the non-reacting case before the onset of low temperature reactions. At 0.4 ms ASI most of the mixture with the mixture fraction higher than 0.05 has a temperature around 1000 K; this corresponds to the fully developed cool flame shown in Figs. 5 and 6. The cool flame increases the temperature by around 150 K at the stoichiometric mixture ($Z_{st} = 0.045$), and increases the temperature by about 400 K at the mixture of 0.2. The scatter plot at 1.2 ms ASI in the reacting case shows that the flow field can be divided into two parts separated by the axial position of lift-off. Combustion in the flow field above the lift-off (z>23 mm in the figure) exhibits a classic structure of a diffusion flame with the peak temperature at the stoichiometric mixture fraction of 0.045; combustion in the flow field below the lift-off shows a developed cool flame structure, which is evidenced by the similarity of the structure to that at 0.4 ms, or 0.325 ms ASI.

Figure 8 shows the time-averaged profiles of mixture fraction at two axial positions. The predicted profiles of mixture fraction are fairly comparable to the experimental measurement. Both the cool flame (at $z = 17.85$ mm) and lifted diffusion flame (at $z = 30$ mm) result in a higher mixture fraction, and the profile of mixture fraction becomes wider than that in the non-reacting case, owing to the spread of fuel jet in the radial direction as discussed earlier.

A probability density function (PDF) of mixture fraction is computed to examine the distribution of the mass originated from the fuel. The PDF is defined as

$$p(Z) = \frac{\sum_{i=1}^{N_{cell}} \tilde{\rho}_i \tilde{Z}_i V_i \alpha_i}{\Delta Z \sum_{i=1}^{N_{cell}} \tilde{\rho}_i \tilde{Z}_i V_i}, \quad \alpha_i = \begin{cases} 1 , & \tilde{Z}_i \in (Z - \Delta Z/2, Z + \Delta Z/2] \\ 0 , & else \end{cases} \tag{19}$$

where V_i is the volume of the i-th mesh cell; $\tilde{\rho}_i$ is the density; N_{cell} is the total number of the cells in the domain. $\Delta Z = 0.005$ is the interval of Z used. As shown in Fig. 9,

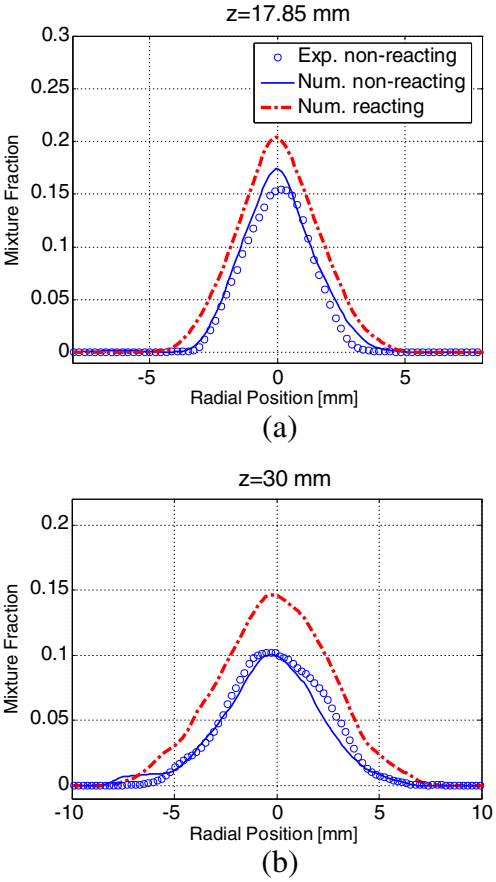

Fig. 8 Mean mixture fraction along the radial direction. Experimental data are taken from Ref. [9]

before the onset of high temperature ignition (e.g., at 0.4 ms ASI), the difference in the distributions of the mass originated from the fuel (i.e. mixture fraction) in the reacting and non-reacting sprays is relatively small. The higher PDF (for mixture fraction greater than 0.3) in the reacting case is owing to the temperature increase from the cool flame, which enhances the evaporation of the liquid fuel. The PDFs are fairly different during the mixing controlled diffusion flame period (i.e. 1.2 ms ASI), in particular for the mixtures around the stoichiometric mixture fraction. Owing to combustion heat release more mixture falls into the fuel-rich side as well as the fuel-lean side, resulting in a much lower PDF around the stoichiometric mixture.

The spatially averaged mean fields of velocity and gas density around the jet have been obtained by density-weighted averaging along the azimuthal direction at the instance of 1.2 ms ASI. The averaged density and flow streamlines are shown in Fig. 10. Thermal expansion due to combustion heat release yields a density much lower in the high temperature gas above the lift-off height than that in the surrounding gas and the corresponding one in the non-reacting case. Similar to the experimental studies [5, 6, 34], the gas velocity field around the spray jet can be divided into three zones. The first zone is close to the injector nozzle, where the surrounding gas is aspirated into the jet flow by the ejection effect of the spray; the second zone is characterized by the recirculation at the downstream of the first zone; the

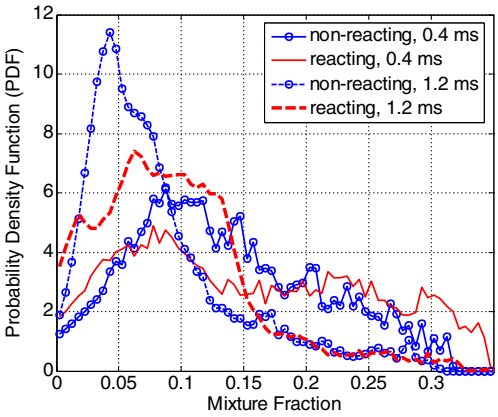

Fig. 9 PDF of mixture fraction at different times

last zone is on the tip of the fuel jet, where the surrounding gas is pushed away from the fuel jet boundary. It is seen that combustion affects the distribution of the streamlines in the flow field. Thermal expansion due to combustion not only improves the penetration of the jet tip but also enhances the flow recirculation towards upstream. The change of the velocity field is noticeably affecting the air entrainment of the jet, which will be discussed later.

Figures 11 and 12 show the time averaged air mass flow rate in the jet and mixing efficiency along the jet axis between 1.0 ms and 2.0 ms ASI. The air mass flow rate in the jet is defined as the mass flow rate of the gas that is originated from the ambient gas inside the jet boundary; the jet boundary is defined by the stoichiometric mixture. The time-average operation was carried out on the section between z=0 mm and z=30 mm, where the flow and mixing are in statistic steady state during this period. The local air flow rate is the cumulative entrainment rate upstream of the position; the gradient of air flow rate along the axial direction is the local entrainment rate. The mixing efficiency is defined as [35],

$$\eta_{mix} = \frac{\int (\tilde{\rho}\tilde{u}_z\tilde{Z}\tilde{\phi}')dxdy}{(\tilde{\rho}\tilde{u}_z\tilde{Z})dxdy}, \ \tilde{\phi}' = \begin{cases} 1, & (\tilde{\phi} \le 1) \\ 1/\tilde{\phi}, & (\tilde{\phi} > 1) \end{cases} \tag{20}$$

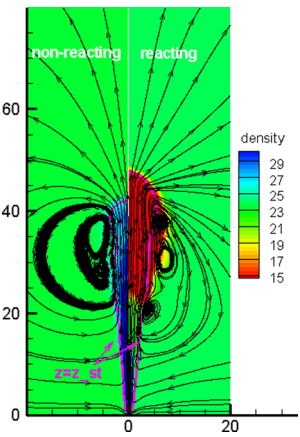

Fig. 10 Mean density and streamlines of the mean flow at 1.2 ms ASI

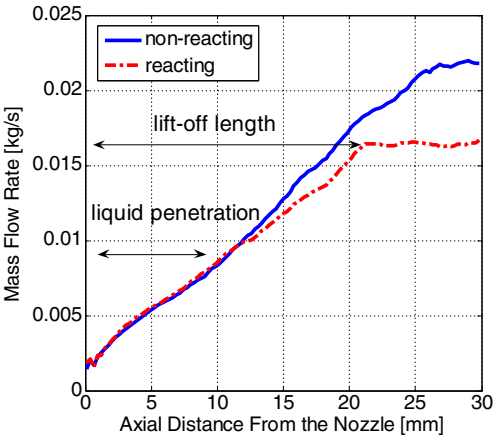

Fig. 11 Time-averaged mass flow rate of air inside the jet between 1.0 ms 2.0 ms ASI

where $\tilde{\phi}$ is the local equivalence ratio defined as

$$\tilde{\phi} = \frac{\tilde{Z}/(1-\tilde{Z})}{Z_{st}/(1-Z_{st})} \tag{21}$$

where $Z_{st}(= 0.045)$ is the stoichiometric mixture fraction. It is shown that the air entrainment from z = 10 mm to z = 21 mm on the axial direction is almost the same in non-reacting and reacting cases. This section corresponds to the evaporating region (within the liquid penetration length in Fig. 2). Figure 12 shows that the mixing efficiency in evaporating region is a little lower in the reacting case; this is owing to the faster evaporation rate due to the cool flame. Downstream the evaporating region, the mass flow rate of the vapor fuel should be the same between the non-reacting and reacting cases due to the same injection rate. In the region from z=10 mm to z=21 mm, which corresponds to the cool flame region upstream the lifted diffusion flame, both the air flow rate and mixing efficiency are slightly lower in the reacting case. This indicates that the cool flame reduces air entrainment to the jet. Further downstream, the air flow rate and mixing efficiency are much lower in the reacting case; the constant air flow rate in the reacting case indicate that there is almost no air

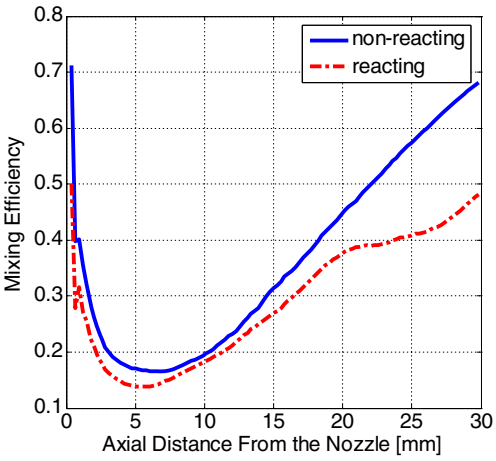

Fig. 12 Mean mixing efficiency during the time interval from 1.0 ms to 2.0 ms ASI

to be entrained into the jet from the side surface of the jet downstream of the lift-off. This explains the higher mixture fraction in the reacting case on the axis of the fuel jet, cf. Fig. 8.

4 Conclusions

Mixing of fuel with ambient air in reacting and non-reacting sprays is investigated using large eddy simulation. It is shown that the mixture in the non-reacting case falls to a quadratic relation between the temperature and mixture fraction due to the evaporation of the liquid fuel; the mixture in the reacting case has a similar temperature distribution before the onset of low temperature reactions (cool flame). The cool flame increases the local temperature of the mixture; hence, it affects the evaporation rate of the liquid fuel.

The penetration of vapor fuel in the reacting case is slightly longer than that in the non-reacting cases in the later stage of the transient spray; in the earlier stage the penetration lengths in the reacting and non-reacting cases are fairly comparable. The liquid phase penetration is shorter in the reacting case due to the faster evaporation rate than that in the non-reacting case owing to the cool flame. The spreading of vapor fuel in radial direction is rather different in the reacting and non-reacting cases. This is owing to the difference in the radial velocity, which is noticeably affected by combustion heat release.

Both the lifted flame and the cool flame can increase the temperature and decrease the density of the mixture. The lifted flame has a significant effect on the air entrainment and mixing owing to the heat release; it modifies the velocity field around the spray, and prevents the ambient gas from being entrained into the jet on the side surface of the jet. This results in a lower entrainment rate of air and slower mixing in the reacting sprays. The cool flame upstream the lifted flame can reduce the air entrainment and slow down the mixing between the vapor fuel and the ambient gas; however, its effect is much smaller than that of the lifted flame.

Acknowledgments This work was supported by the Swedish research funding organizations (CeCOST, KCFP and VR), and partly sponsored by Scania CV AB through a FFI project. Cheng Gong was sponsored by China Scholarship Council (CSC). The computations were performed using the computer facilities provided by the Centre for Scientific and Technical Computing at Lund University (LUNARC), the High Performance Computing Center North at Umeå University (HPC2N), and the Center for Parallel Computers at Royal Institute of technology (PDC).

Appendix A: Sub-models for the discrete phase

A1. Heat-transfer and vaporization models

The liquid droplet receives the energy from the gas, which is used to increase the liquid temperature and overcome the latent heat of evaporation in order to evaporate the fuel. The equation for the heat transfer to the liquid parcel is given by

$$m_p \frac{dh_p}{dt} = \dot{m}_p h_v(T_p) + \pi d_p \kappa Nu(T - T_p) f, \tag{A1}$$

$$f = \frac{z}{e^z - 1}, z = -\frac{c_{p,v}\dot{m}_p}{\pi d_p \kappa Nu}, \tag{A2}$$

where m_p is the mass of the parcel, $\dot{m}_p$ is the evaporation rate, h_p is the enthalpy of the parcel, $d_p$is the diameter of the droplets in the parcel, h_v is the fuel vapor specific enthalpy at

the parcel temperature T_p, T is the local ambient temperature. κ is the thermal conductivity, $c_{p,v}$ is the specific heat capacity of the vapor, and Nu is the Nusselt number. Various correlations for the Nusselt number are reviewed by Gosman and Clerides [36]. The correlation used here is

$$Nu = 2.0 + 0.6Re_p^{1/2}\mathrm{Pr}^{1/3}, \tag{A3}$$

where the Prandtl number is defined as $\mathrm{Pr} = \mu\frac{c_p}{\kappa}$. All properties are evaluated using the film temperature, i.e., the 1/3-rule,

$$T_f = \frac{2T_p + T}{3} \tag{A4}$$

Solving Eq. A1 in practice is performed by introducing two characteristic heat transfer relaxation times, τ_h and τ_e, defined as

$$\tau_h = \frac{m_p c_{l,p}}{\pi d_p \kappa Nu}, \quad \tau_e = -\frac{m_p}{\dot{m}_p}, \tag{A5}$$

where $c_{l,p}$ is the specific heat for the liquid. Eq. A1 is then rewritten to as

$$\frac{dT_p}{dt} = \frac{T - T_p}{\tau_h} f - \frac{1}{c_{l,p}} \frac{h_v(T_p)}{\tau_e}. \tag{A6}$$

The condensation process is not significant in diesel spray; thus, the only transfer of mass is from the liquid phase to the gas phase. Evaporation rate for a parcel with the temperature below the boiling temperature is given by

$$\dot{m}_p = \frac{dm_p}{dt} = -n\pi d_p D\rho_v Sh \ln\left(\frac{p - p_v}{p - p_{v,s}}\right), \tag{A7}$$

where n is the number of droplets in the parcel; $\rho_v$and $p_v$are the fuel vapor density and fuel vapor pressure close to the droplets surface. $p_{v,s}$ is the saturated vapor pressure. The effect of the relative velocity on the evaporation rate is accounted for using the Ranz-Marshall correlation,

$$Sh = 2.0 + \frac{3}{5} Re^{1/2} Sc^{1/3}, \tag{A8}$$

where Sh is the Sherwood number. The evaporation relaxation time is then given by

$$\tau_e = \frac{m_p}{\pi d_p D Sh \rho_v \ln\frac{p - p_v}{p - p_{v,s}}}. \tag{A9}$$

The evaporation rate, Eq. A7, is rewritten to as

$$\frac{dm_p}{dt} = -\frac{m_p}{\tau_e}. \tag{A10}$$

When the liquid droplets start boiling, the vapor pressure rises above the ambient pressure; Eq. A7 is then no longer valid. The evaporation rate at boiling point is controlled by the heat transfer; therefore the boiling mass transfer rate is given by

$$\frac{dm_p}{dt} = -\frac{\pi D\kappa Nu}{c_{p,v}} \ln\left(\frac{c_{p,v}}{h_v}(T - T_p) + 1\right). \tag{A11}$$

The relaxation time in Eq. A10 should be replaced by a boiling relaxation time,

$$\tau_e = \tau_{boil} = \frac{d_p^2 \rho_p c_{p,v}}{2\kappa Nu \ln\left(\frac{c_{p,v}}{h_v}(T - T_p) + 1\right)} \tag{A12}$$

For more details of heat transfer and evaporation models, see Ref. [37] and references herein.

A2. Primary breakup model

Huh-Gosman model [15] is used for modeling the primary breakup of the liquid fuel. This model assumes that parcels (blobs) are primarily injected into the computational domain with the same size as nozzle diameter and their velocity is a function of injected mass flow rate. This model is able to take into account both Kelvin-Helmholtz and turbulence induced breakup on the jet surface. The diameter reduction of the injected parcels is obtained from

$$\frac{d}{dt}d_p = -C_5\frac{L_a}{D_a} \tag{A13}$$

where C_5 is a model constant; L_a and D_a are the characteristic breakup length and time scales and their values are a function of the geometry of the injection system, turbulence decay within the jet and Kelvin-Helmholtz instabilities. At the nozzle exit, the spray angle is estimated from

$$\tan\ \frac{\alpha}{2}\Big) = \frac{L_a/D_a}{U} \tag{A14}$$

where U is the droplet velocity at the nozzle exit.

The time scale of atomization is assumed to be a linear function of two time scales,

$$\tau_a = C_1\tau_t + C_4\tau_w \tag{A15}$$

where τ_t is the turbulent time scale and τ_w is the wave growth time scale. The length scale of the turbulence L_t is assumed to be the dominant length scale of the atomization process; hence, the atomization length scale L_a and the wavelength scale L_w are expressed as,

$$L_a = C_2 \cdot L_t \tag{A16}$$

$$L_w = C_3 \cdot L_t \tag{A17}$$

Assuming that half a surface wave is detached as secondary droplet from the jet, L_a and L_w are related to as,

$$L_a = 0.5L_w \tag{A18}$$

Therefore,

$$C_3 = 2C_2 \tag{A19}$$

The wave growth time scale τ_w is estimated according to the Kelvin-Helmholtz instability theory for an in viscid liquid on an infinite plane:

$$\tau_w = \left[\frac{\rho_l \cdot \rho}{\rho_l + \rho} \cdot \left(\frac{u}{L_w}\right)^2 - \frac{\sigma_l}{(\rho_l + \rho)\, L_w^3}\right]^{-0.5} \tag{A20}$$

where ρ_l and ρ are respectively the densities of the liquid fuel and the local ambient gas, respectively; σ_l is the surface tension, and u is the gas phase velocity.

On the basis of the above assumptions, the turbulent length scale and turbulent time scale are the key parameters in the atomization process. L_t and τ_t are expressed as:

$$L_t = C_\mu^{0.75} \cdot \frac{K_{avg}^{3/2}}{\varepsilon_{avg}} \tag{A21}$$

$$\tau_t = C_\mu^{0.75} \cdot \frac{K_{avg}}{\varepsilon_{avg}} \tag{A22}$$

where K_{avg} and ε_{avg} are the liquid averaged turbulent kinetic energy and its dissipation rate at nozzle exit, respectively. These parameters are estimated considering a simple pressure drop balance along the nozzle downstream length [38]. Here, C_μ is set to 0.09 [15].

New droplets are created from the parent droplets in a parcel when the amount of stripped mass is higher than 20 % of the parent parcel mass.

In the present simulation, the parameters for the Huh-Gasman model are set as:

$$C_1 = 3.0,\ C_3 = 1.0,\ C_4 = 3.0 \text{ and } C_5 = 10.$$

A3. Secondary breakup model

The Kelvin-Helmholtz (WAVE) model [16] is used to model the secondary breakup of the droplets. In this model, the diameter of the parcels reduces as

$$\frac{d}{dt}d_p = -\frac{d_p - d_{new}}{\tau_{bu}}, \text{ with } \tau_{bu} = 1.894 B_1 \frac{d_{new}}{\Omega \cdot \Lambda}, \text{ and } d_{new} = B_0 \cdot \Lambda, \tag{A23}$$

where d_{new} is the diameter of the new child droplet, and τ_{bu} is the breakup time. Ω and Λ represent the most unstable growth rate and wave number [16],

$$\Lambda = 0.02 \frac{r_p(1 + 0.45Oh^{1/2})(1 + Ta^{0.7})}{(1 + 0.865We^{1.67})} \tag{A24}$$

$$\Omega = \frac{0.34 + 0.38We^{3/2}}{(1 + Oh)(1 + 1.4Ta^{0.6})} \sqrt{\frac{\sigma}{\rho_l r_p^3}} \tag{A25}$$

where σ is the surface tension of the liquid fuel; r_p is the radius of the droplet. $We = \rho \left|\vec{u}_{rel}\right|^2 r_p/\sigma$ is the Weber number, which is calculated based on the gas density ρ; $Oh = \sqrt{We}/Re_p$ is the Ohnesorge number; $Ta = Oh\sqrt{We}$ is the Taylor number.

In the present simulation, the parameters for WAVE model are set to: $B_0 = 0.61,\ B_1 = 6.0$. The Weber number is used to switch the parcel between primary breakup and secondary breakup regime. Since parent droplets continuously reduce their diameter because of atomization, they will considerably reduce their Weber number. The critical Weber number for primary breakup is set to as 80; the critical Weber number for the secondary breakup is set to as 6. When the Weber number falls below the threshold of 80, the parent droplets are taken into consideration in the secondary breakup model; when the Weber number falls below 6, there is no breakup happening.

Appendix B: Chemistry Coordinate Mapping (CCM) approach

The basic idea of the CCM method is to map the thermo-chemistry identical points/ mesh cells in the physical space to a multidimensional phase space made up of temperature,$\tilde{T}$, mass fraction of H-atom,J_H, and a logarithm function of the scalar dissipation rate, $\alpha = \log_{10}(\nabla J_H \cdot \nabla J_H + 1)$. The mass fraction of H-atom is defined as

$$J_H = \sum_{k=1}^{Ns} \frac{W_H}{W_k} \beta_{H,k} \tilde{Y}_k, \tag{26}$$

where W_H and W_k are the atomic and molecular weights of hydrogen and the kth species, respectively. $\beta_{H,k}$ is the number of H-atom in the $k$thspecies. Ns is the total number of species in the mixture. The phase space $(J_H, \tilde{T}, \alpha)$ is discretized uniformly into N_J, N_T and N_α intervals in the J_H, $\tilde{T}$ and α coordinate, respectively. The (i, j, k) cell in the physical domain is mapped to the (l, m, q) zone in the $(J_H, \tilde{T}, \alpha)$ space. In the present reacting case, after sensitivity test, the following setup is used, $J_H = 1000,\ N_T = 1000$ and $N_\alpha = 100$.

The mean values of the variables in each phase space zone are determined and used as the initial conditions for integrating the reaction rates at time t_n, i.e.,

$$\hat{Y}_k(l, m, q, t_n) = \frac{1}{N_c} \sum_{(i,j,k)\to(l,m,q)} \tilde{Y}_k(i, j, k, t_n), \tag{27}$$

where N_c is the total number of cells in the physical space that are mapped to (l, m, q) zone. The error due to the mapping for the (i, j, k) cell is

$$\varepsilon_{\tilde{Y}_k(i,j,k,t_n)} = \frac{\left|\tilde{Y}_k(i, j, k, t_n) - \hat{Y}_k(l, m, q, t_n)\right|}{\hat{Y}_k(l, m, q, t_n)}. \tag{28}$$

"Ill" cells in physical space are those that

$$\varepsilon_{\tilde{Y}_k(i,j,k,t_n)} > \varepsilon_{acp}, \tag{29}$$

where ε_{acp} is an error threshold set to 10^{-4} in this study. To ensure the accuracy of the mapping procedure these ill cells are treated as individual zones in the phase space.

Once the initial condition is determined for all zones in the phase space, integration of the chemical reaction rates is performed in each phase space zone to obtain the mean reaction rates. The results are then mapped back to the cells in the physical space. These reaction rates are then integrated together with the transport terms in the governing equations. More details of the CCM approach are referred to Refs. [19, 25–28].

References

1. Ricou, F.P., Spalding, D.B.: Measurements of entrainment by axisymmetrical turbulent jets. J. Fluid. Mech. **11**(01), 21–32 (1961). doi:10.1017/S0022112061000834.
2. Sasaki, S., Akagawa, H., Tsujimura, K.: A Study on Surrounding Air Flow Induced by Diesel Sprays. SAE Technical Paper 980805 (1998)
3. Ishikawa, N., Zhang, L.: Characteristics of Air-entrainment in a Diesel Spray. SAE Technical Paper 1999-01-0522 (1999)
4. Rhim, D.R., Farrell, P.V.: Characteristics of Air Flow Surrounding Non-Evaporating Transient Diesel Sprays. SAE Technical Paper 2000-01-2789 (2000)
5. Rhim, D.R., Farrell, P.V.: Air Flow Characteristics Surrounding Evaporating Transient Diesel Sprays. SAE Technical Paper 2002-01-0499 (2002)
6. Rhim, D.R., Farrell, P.V.: Air Flow Surrounding Burning Transient Diesel Sprays. SAE Trans. **105**(3), 82–111 (1996)
7. Naber, J.D., Siebers, D.L.: Effects of Gas Density and Vaporization on Penetration and Dispersion of Diesel Sprays. SAE Technical Paper 2002-01-2668 (2002)
8. Siebers, D.: Recent Developments on Diesel Fuel Jets Under Quiescent Conditions. In: Arcoumanis, C., Kamimoto, T. (eds.): Flow and Combustion in Reciprocating Engines. Experimental Fluid Mechanics, pp. 257–308. Springer Berlin Heidelberg (2009)
9. Engine Combustion Network: http://www.sandia.gov/ecn/dieselSprayCombustion.php (2014)
10. Zhou, L., Xie, M.Z., Jia, M., Shi, J.R.: Large eddy simulation of fuel injection and mixing process in a diesel engine. Acta Mechanica Sinica **27**(4), 519–530 (2011). doi:10.1007/s10409-011-0485-1.
11. Solsjö, R., Bai, X.S.: Injection of Fuel at High Pressure Conditions: LES Study. SAE Technical Paper 2011-24-0041 (2011)
12. Menon, S.: Subgrid combustion modelling for large-eddy simulations. Int. J. Engine Res. **1**(2), 209–227 (2000). doi:10.1243/1468087001545146.
13. Bharadwaj, N., Rutland, C.J., Chang, S.: Large eddy simulation modelling of spray-induced turbulence effects. Int. J. Engine Res. **10**(2), 97–119 (2009). doi:10.1243/14680874jer02309.
14. O'Rourke, P.J.: Statistical properties and numerical implementation of a model for droplet dispersion in a turbulent gas. J. Comput. Phys. **83**(2), 345–360 (1989)

15. Huh, K., Gosman, A.: A phenomenological model of diesel spray atomization. In: Proceedings International Conference on Multiphase Flows (1991)
16. Reitz, R.D.: Modeling atomization processes in high-pressure vaporizing sprays. Atomization Spray Technol. **3**(4), 309–337 (1987)
17. Baumgarten, C.: Mixture formation in internal combustion engines. Springer (2006)
18. D'Errico, G., Lucchini, T., Contino, F., Jangi, M., Bai, X.S.: Comparison of well-mixed and multiple representative interactive flamelet approaches for diesel spray combustion modelling. Combust. Theory Model **18**(1), 65–88 (2014)
19. Jangi, M., D'Errico, G., Bai, X.S., Lucchini, T.: Numerical Simulation of the ECN Spray A Using Multidimensional Chemistry Coordinate Mapping: n-Dodecane Diesel Combustion. SAE Technical Paper 2012-01-1660 (2012)
20. Jangi, M., Bai, X.S.: On the large eddy simulation of evaporating diesel spray. 8th Mediterranean Combustion Symposium, Çesme, İzmir, Turkey (2013)
21. Pei, Y.J., Hawkes, E.R., Kook, S.: A comprehensive study of effects of mixing and chemical kinetic models on predictions of n-heptane jet ignitions with the PDF method. Flow Turbul. Combust. **90**(2), 249–280 (2013)
22. Bajaj, C., Ameen, M., Abraham, J.: Evaluation of an Unsteady Flamelet Progress Variable Model for Autoignition and Flame Lift-Off in Diesel Jets. Combust. Sci. Technol. **185**, 454–472 (2012)
23. Bhattacharjee, S., Haworth, D.C.: Simulations of transient n-heptane and n-dodecane spray flames under engine-relevant conditions using a transported PDF method. Combust. Flame **160**(10), 2083–2102 (2013)
24. Pei, Y.J., Hawkes, E.R., Kook, S.: Transported probability density function modeling of the vapour phase of an n-heptane jet at diesel engine conditions. Proc. Combust. Inst. **34**, 3039–3047 (2013)
25. Jangi, M., Yu, R., Bai, X.S.: A multi-zone chemistry mapping approach for direct numerical simulation of auto-ignition and flame propagation in a constant volume enclosure. Combust. Theory Model **16**(2), 221–249 (2011)
26. Jangi, M., Lucchini, T., D'Errico, G., Bai, X.S.: Effects of EGR on the structure and emissions of diesel combustion. Proc. Combust. Inst. **34**, 3091–3098 (2013)
27. Jangi, M., Bai, X.S.: Multidimensional chemistry coordinate mapping approach for combustion modelling with finite-rate chemistry. Combust. Theory Model **6**, 1109–1132 (2012). doi:10.1080/13647830.2012.713518.
28. Jangi, M., Yu, R., Bai, X.S.: Development of Chemistry Coordinate Mapping Approach for Turbulent Partially Premixed Combustion. Flow Turbul. Combust. **90**(2), 285–299 (2013). doi:10.1007/s10494-012-9412-1.
29. Solsjö, R., Jangi, M., Chartier, C., Andersson, Ö., Bai, X.S.: Lift-off and stabilization of n-heptane combustion in a diesel engine with a multiple-nozzle injection. Proc. Combust. Inst. **34**, 3031–3038 (2013)
30. Jangi, M., Zhao, X., Haworth, D., Bai, X.-S.: Stabilization and liftoff length of a non-premixed methane/air jet flame discharging into higth temperature environment: an accelerated transport PDF method. Combust. Flame (2014). (accepted)
31. The open source CFD toolbox available at http://www.openfoam.com (2014)
32. Som, S., Longman, D.E., Luo, Z., Plomer, M., Lu, T.: Three Dimensional Simulations of Diesel Sprays Using n-Dodecane as a Surrogate. Fall Technical Meeting of the Eastern States Section of the Combustion Institute (2011)
33. Musculus, M.P.B., Miles, P.C., Pickett, L.M.: Conceptual models for partially premixed low-temperature diesel combustion. Prog. Energy Combust. Sci. **39**(2–3), 246–283 (2013)
34. Zhu, J., Kuti, O.A., Nishida, K.: Effects of Injection Pressure and Ambient Gas Density on Fuel - Ambient Gas Mixing and Combustion Characteristics of D.I. Diesel Spray. SAE Technical Paper 2011-01-1819 (2011)
35. Watanabe, J., Kouchi, T., Takita, K., Masuya, G.: Large-Eddy Simulations of Hydrogen and Ethylene Injections into a Supersonic Crossflow. AIAA Paper, 2011–5764 (2011)
36. Gosman, A.D., Clerides, D.: Diesel Spray Modelling: A Review. In: ILASS-Europe Conferences, Florence, Italy (1997)
37. Nordin, N.: Complex chemistry modeling of diesel spray combustion. Ph.D. thesis, Chalmers University of Technology (2001)
38. Lucchini, T., D'Errico, G., Ettorre, D.: Experimental and Numerical Investigation of High-Pressure Diesel Sprays with Multiple Injections at Engine Conditions. SAE Technical Paper 2010-01-0179 (2010)